JACS
JOURNAL OF THE AMERICAN CHEMICAL SOCIETY
pubs.acs.org/JACS
Article

Molecular Self-Gating Inside a Zeolite Catalyst

Zhiqiang Liu,*[,⊥] Caiyi Lou,[⊥] Jiamin Yuan, Xiaomin Tang, Yuzhou Fan, Ji Qi, Rui Zhang, Peng Peng, Guoliang Liu, Shutao Xu,* and Anmin Zheng*

Cite This: J. Am. Chem. Soc. 2025, 147, 6126–6136
Read Online
ACCESS | Metrics & More | Article Recommendations | Supporting Information

ABSTRACT: Diffusion is a ubiquitous process that is strongly correlated with concentration. Based on developed three-dimensional free energy and a continuous-time random-walk coarse-graining method, we found the optimal diffusion pathway under confinement, determined all diffusional energy barriers, and identified the major units of zeolite where molecular diffusion is limited. Interestingly, a novel diffusion mechanism was determined in the nanopore of a zeolite catalyst by molecular dynamics simulation, pulsed field gradient, and 2D exchange spectroscopy (EXSY) NMR experiments. We describe a "molecular self-gating effect" that effectively predominates the diffusion process in cage-type (e.g., RHO and MER) zeolites through a "traffic jam" and a "smooth traffic" process. Initially, transport is hindered by molecules forming a gate (traffic jam); then, as the number of molecules reaches a certain threshold, diffusion increases rapidly due to the synergistic collisions of aggregated molecules upon the gate (smooth traffic). This unique diffusion behavior is observed here for the first time and illustrates a microscopic mechanism dictated by the molecular self-gating effect in a confined space. The exploitable diffusion disclosed herein should shed new light on the fundamental understanding of transport, as well as enrich diffusion behavior under confinement.

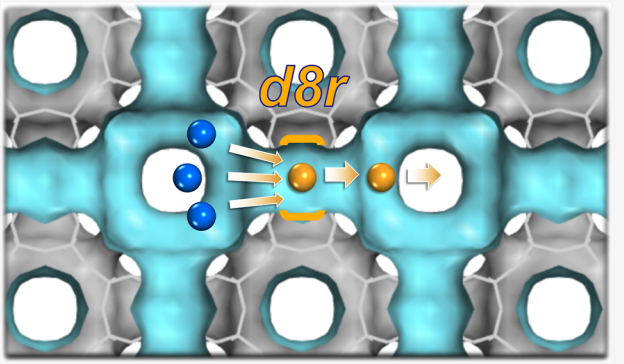

1. INTRODUCTION

Diffusion of mass, heat, and momentum, which ranges from the microscopic to macroscopic, is encountered throughout the world and plays an important part in our lives.[1−3] This is particularly true of the channels of nanopores, such as metal−organic frameworks (MOFs) and zeolites.[4−8] MOFs are a class of crystalline nanoporous materials formed by the assembly of inorganic nodes and organic linkers,[9] whereas zeolites are microporous crystalline aluminosilicates.[10] The constrained channels of nanoporous materials and their high inner-surface area facilitate the interaction of molecules and ions, thereby promoting applications in matter upgrading, including catalysis, separation, purification, and ion exchange.[11−13]

Diffusion is strongly correlated with concentration during the spreading process in confined environments.[14−18] To date, five different kinds of diffusion behavior as a function of concentration have been observed.[19] For example, Smit et al. studied the loading dependence of self-diffusion in one-dimension channel zeolites (e.g., AFI, MTW, and LTL) and found that the diffusion coefficient monotonically decreases as loading increases (see Type 1 in Figure 1), which is similar to that in intersecting channel-type zeolites (e.g., MFI, BOG, BEC, and ISV).[14,16,20] Meanwhile, several unsaturated hydrocarbons[21,22] and small polar water molecules[23] in zeolite NaX exhibited Type 2 (initial constant self-diffusion coefficients that decrease at high loading) and Type 3 (monotonically increasing self-diffusion coefficients that maintain a threshold upon further increasing concentrations) diffusion, respectively. An example of Type 4 diffusion was shown by Schmid et al. where the diffusion of benzene in MOF-5 first increased and then decreased as loading increased.[24] In addition, the self-diffusion coefficients of ethane and propane in zeolite Na_4Ca_4A show a monotonical increase with increasing concentration (see Type 5 in Figure 1).[19] Overall, the relationship between diffusion and concentration is very complex: it is not only related to the size of the adsorbed molecules and the pore size of porous materials but also depends on the interaction between molecules and the framework of porous materials, as well as intermolecular interactions.[25,26] Therefore, more generalized methods to quantitatively correlate the diffusion and structure of porous materials, taking into account loading, are urgently needed.

From the perspective of fundamental research and practical applications, novel molecular transport will enrich the present diffusion behavior as well as increase industrial productivity.[11] For example, Ghorai et al. found the "levitation effect" for diffusion anomaly as a function of molecular length for linear

Received: December 8, 2024
Revised: January 26, 2025
Accepted: January 31, 2025
Published: February 11, 2025

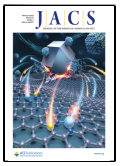

https://doi.org/10.1021/jacs.4c17510
J. Am. Chem. Soc. 2025, 147, 6126−6136

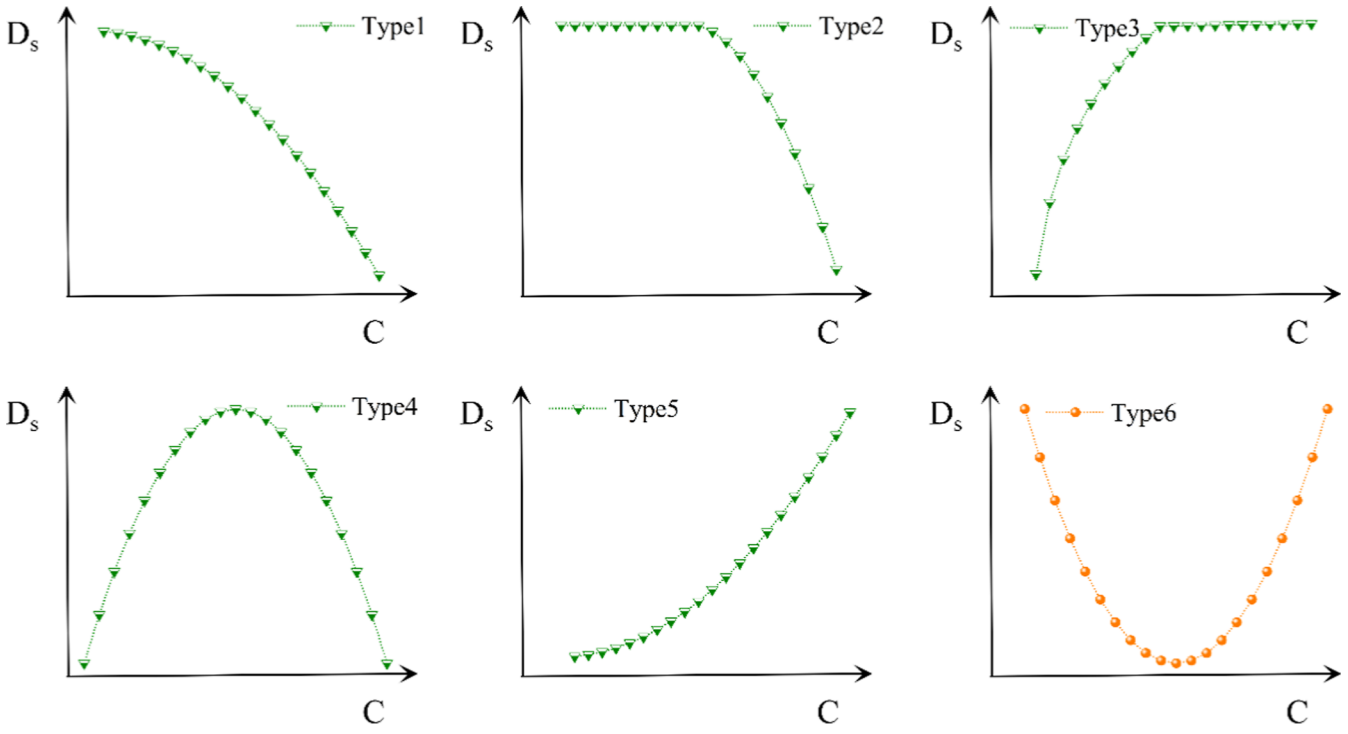

Figure 1. Types of the concentration dependence of self-diffusion coefficient. Types 1−5 are found in the literature, and a new type (Type 6) is proposed in this work. D_s, self-diffusion coefficient; C, concentration.

molecules,[27] and Nag et al. illustrated the efficacy of the levitation effect for separating real mixtures of both linear *n*-pentane and its branched isomer.[28] Here, a novel diffusion behavior as a function of loading (see Type 6 in Figure 1) was detected, where the diffusion decreases and then increases inside RHO- and MER-type zeolites due to a "molecular self-gating mechanism". In addition, by combining three-dimensional (3D) diffusion free energy and continuous-time random-walk (CTRW) coarse graining, we developed new methods that can quantitatively correlate diffusion and zeolite topology.

2. RESULTS AND DISCUSSION

2.1. Diffusion Behavior. The diffusion behaviors of molecules inside the confined channel are strongly correlated with the zeolite framework, as Beerdsen et al. showed that Type 1 diffusion and Type 4 diffusion are prone to occur in channel/intersecting channel-type and cage-type zeolites, respectively.[16] Figure 2a shows the 3D channels of RHO cage-type zeolite, which possess Linde type A (*lta*) cages connected with each other by a double eight-member ring (*d8r*) (Figure S1a in Supporting Information).[29] To determine the following unique diffusion behaviors, we also investigated the other cage-type zeolite (LTA) that consists of *lta* cages bridged by a single eight-member ring (*s8r*; see Figures 2b and S1b in Supporting Information). Here, we used molecular dynamics (MD) to calculate the self-diffusion coefficient (D_s), which can quantitatively describe the movement of guest molecules inside confined channels.[25] Details of the MD calculations are presented in Computatinal and Experimental Methods. With methane (CH_4) as a model, the D_s of CH_4 inside the RHO at 298 K as a function of loading is plotted in Figure 2c.

Interestingly, a novel kind of diffusion behavior where the D_s first decreases and then increases as the concentration increases is observed for the RHO-type zeolite (see Type 6 in Figure 1). For example, the D_s is 6.5×10^{-10} m^2/s at the loading number of one molecule per cage, and then it monotonically decreases to 0.9×10^{-10} m^2/s at 9 molecules per cage and then again increases to 4.4×10^{-10} m^2/s at 12 molecules per cage (Figure 2c). For comparison, the dependence of D_s on the methane loadings in LTA zeolite is also shown in Figure 2c; D_s is 22.7×10^{-10}, 33.7×10^{-10}, and 12.6×10^{-10} m^2/s at loadings of 1, 7, and 10 molecules per cage, respectively. Clearly, D_s first increases and then decreases (see Type 4 in Figure 1), which agrees with the result of Smit et al.[20] It should be noted that the loading-dependent diffusion of molecules in RHO (*lta* and *d8r*) and LTA (*lta* and *s8r*) zeolites is completely reversed, which we ascribe to the difference in composite building units between *d8r* and the *s8r*.

To understand the difference in the type of diffusion of methane molecules in RHO and LTA zeolites, we obtained visual and quantitative information on the diffusion trajectories on the microscopic scale.[30] As shown in Figure 2d, the diffusion of CH_4 in cage-type zeolite has a "jump-like" motion, which includes intracage motions and occasional intercage jumps through eight-member ring. Figure 2e,f shows the representative diffusion trajectories of RHO and LTA in the XY plane during a diffusion time of 100 ns (1 molecule per cage; see Figures S2 and S3 for other planes and loadings), and Figure 2g presents the diffusion radius (R; see Methods in Supporting Information) in RHO and LTA zeolites as a function of loading at 298 K. R first decreases (e.g., R is 152 and 60 Å at 1 and 9 molecules per cage, respectively) and then increases (e.g., R is 141 Å at 12 molecules per cage). However, for LTA zeolites, R first increases and then decreases: R is 281 Å for a single molecule per cage, 369 Å for 7 molecules per cage, and 241 Å for 10 molecules per cage (Figure 2g), and all the diffusion radii are larger than that in RHO. These results agree well with the order of D_s as a function of loading in both

https://doi.org/10.1021/jacs.4c17510
J. Am. Chem. Soc. 2025, 147, 6126−6136

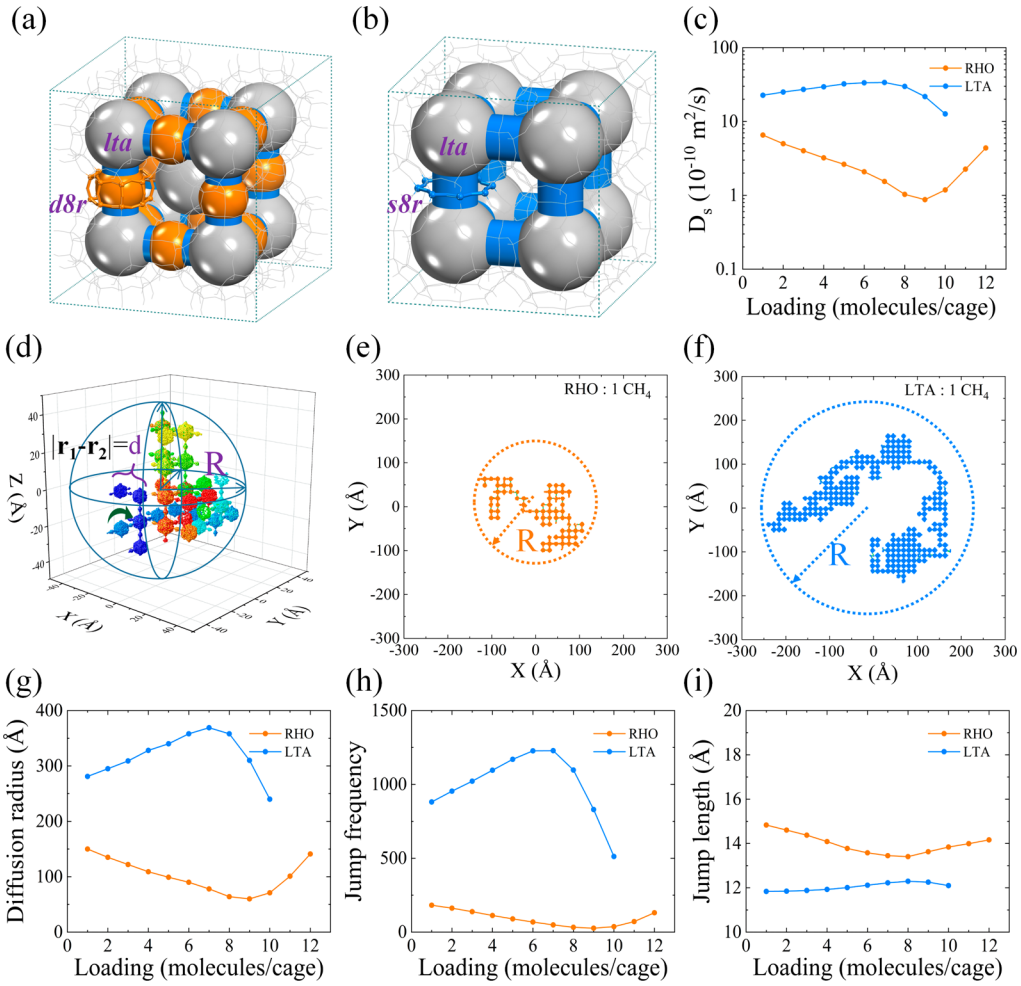

Figure 2. Three-dimensional (3D) channels of (a) RHO-type zeolite, which possesses *lta* cages (silver) and double eight-member ring (*d8r*, orange) structures and (b) LTA-type zeolite, which possesses *lta* cages (silver) and single eight-member ring (*s8r*, blue) structures. (c) Self-diffusivity (D_s) of methane (CH_4) inside RHO and LTA zeolite as a function of loading at 298 K. (d) 3D jump-like diffusion in cage-type zeolite; the trajectories were colored with time proceeding (red−yellow−green−blue). Trajectories of one representative methane diffusion in (e) RHO and (f) LTA zeolite in the *XY* plane at the loading of 1 molecule per cage during 100 ns. (g) Diffusion radius (R), (h) jump frequency, and (i) jump length in zeolites as a function of loading at 298 K.

RHO and LTA zeolites, further indicating that the diffusion trajectories can be used to analyze the diffusion behaviors.

Furthermore, the diffusion in a cavity-type zeolite could be regarded as a "hurdle race" that is directly determined by jump frequency (f) and jump length (d) between two neighboring basins or cages.[30] Generally, high f and long d values between two cages lead to fast diffusion with a longer diffusion radius. As presented in Figure 2i and Table S3 in Supporting Information, the d does not change much as the loading is varied (ca. 14 and 12 Å for RHO and LTA, respectively), indicating that d is not the main factor for the diffusion differences. Fortunately, the trend of the f (Figure 2h and Table S3 in Supporting Information) is identical to that of the diffusion coefficient (Figure 2c) and diffusion radius (Figure 2g). For example, during 100 ns diffusion time, f is 181, 27, and 131 at the loading number of 1, 9, and 12 molecules per cage, respectively, in RHO zeolite (first a decrease and then an increase), whereas f is 881, 1128, and 551 at the loading number of 1, 7, and 10 molecules per cage (Figure 2h and Table S4 in Supporting Information), respectively, in LTA zeolite (first an increase and then a decrease). Overall, this suggests that the diffusion in cage-type zeolites can be regarded as a "hurdle race", and the loading-dependent diffusion is mainly due to the jump frequency between two neighboring cages.

2.2. Interaction Energy. Our observations suggest that the eight-membered ring affects diffusion by the jump frequency. Thus, we ascribe the unique movement of guest molecules inside the confined channels of the RHO to interaction energy and free energy, which are important factors affecting diffusion behavior (e.g., diffusion barrier and jump frequency) in different channels.[31] Here, interaction energy is used to study the diffusion properties at low concentrations and allows for a comparative analysis of the diffusion difference in zeolites with different topologies, whereas the free energy analysis is performed to elucidate the mechanism of diffusion upon various loadings in the same zeolite.

Generally, the interaction energy (or adsorption energy) is strongly correlated with the zeolite framework, thus leading to differences in interaction energies due to local-structure variations.[31] The interaction energy profiles of CH_4 in RHO and LTA zeolites are shown in Figure 3c,d and Table S5 in Supporting Information. These values indicate that CH_4 is impeded from attaching to the center (see points A and A′ in

https://doi.org/10.1021/jacs.4c17510
J. Am. Chem. Soc. 2025, 147, 6126−6136

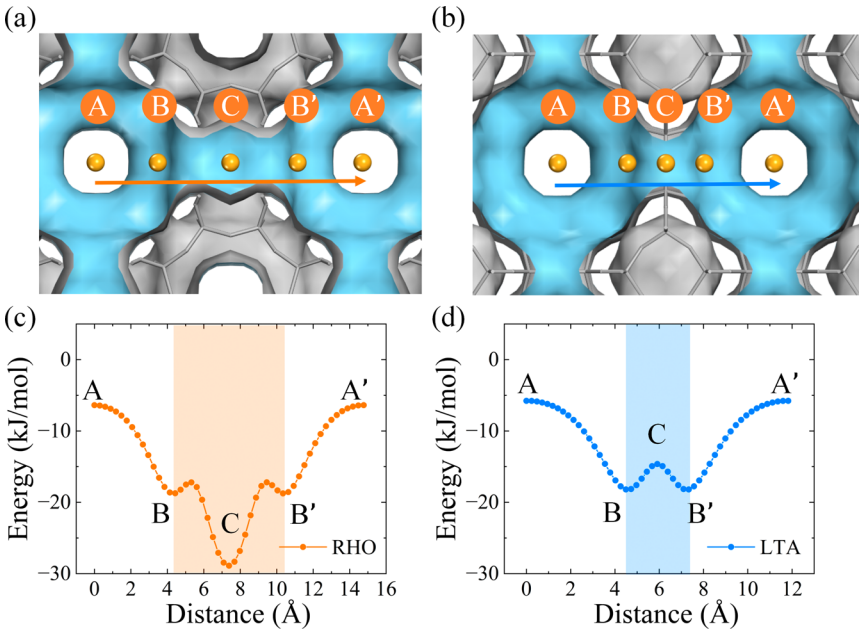

Figure 3. Definition of the methane diffusion pathway (points A to A′) from one cage to another in (a) RHO and (b) LTA zeolites. Interaction energy profiles of methane from one cage to another in (c) RHO and (d) LTA zeolites.

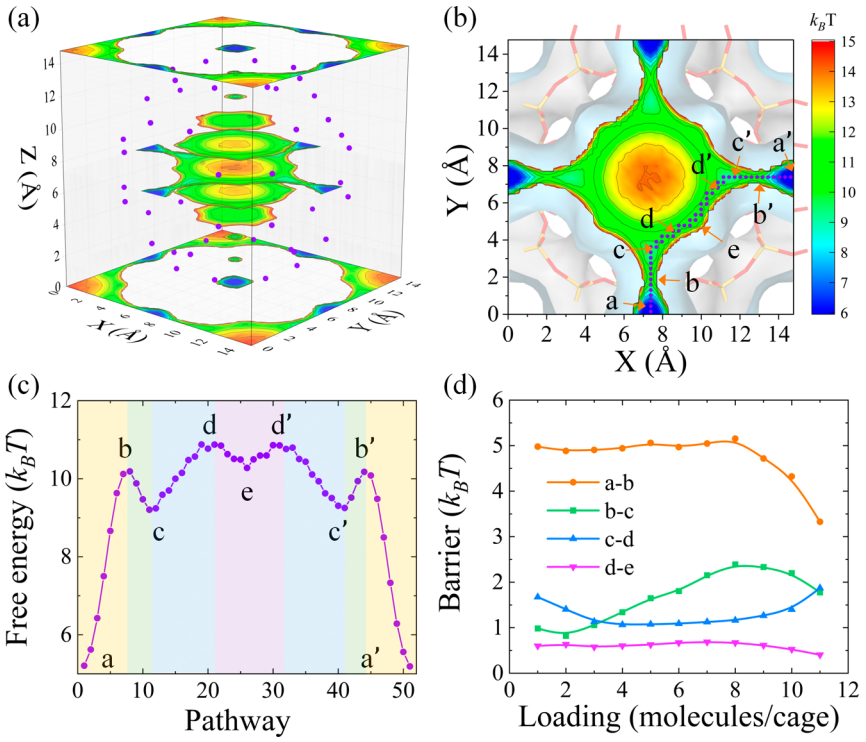

Figure 4. (a) 3D free energy map of diffusion for 1 methane per cage in RHO zeolite. The purple balls represent Si atoms for one cage. (b) 2D free energy of diffusion extracted from 3D free energy map. The blue−green−yellow−red color indicates free energy from low to high, and the purple dots indicate the minimum free energy diffusion path. (c) State of 1D local minimum free energy extracted from 2D free energy map, and (d) free energy barriers for varied loadings in RHO zeolite at 298 K.

Figure 3a,b) due to weak adsorption energy (ca. −6 kJ/mol), but CH_4 tends to locate in the edge of the *lta* cage in both RHO (see points B and B′ in Figure 3a) and LTA (see points B and B′ in Figure 3b) zeolites because of stronger adsorption energy (about −18 kJ/mol). Interestingly, the strongest adsorption point (ca. −29 kJ/mol) is only detected at the center of *d8r* (see point C in Figure 3c) for RHO zeolite, while a low adsorption site is located (ca. −15 kJ/mol) at the center of *s8r* (see point C in Figure 3d). Note that strong adsorption sites slow diffusion, and thus the diffusion of CH_4 in RHO is slower than that in LTA zeolite at low loading. The results show that the existence of *d8r* and *s8r* structures will affect the diffusion behavior by generating different interaction energy profiles.

https://doi.org/10.1021/jacs.4c17510
J. Am. Chem. Soc. 2025, 147, 6126−6136

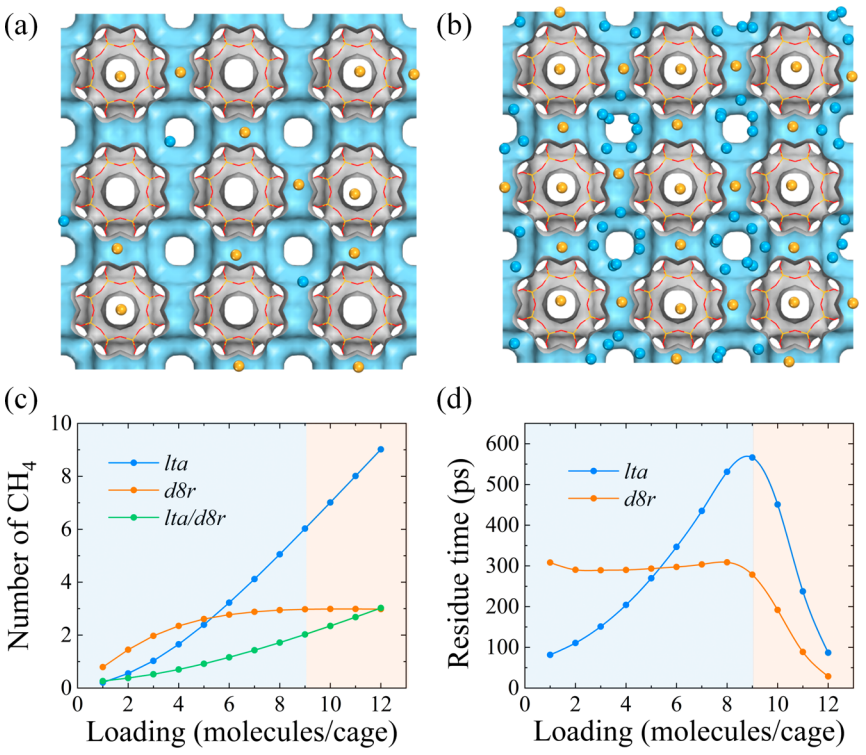

Figure 5. Adsorption sites of CH_4 inside the RHO zeolite at 298 K at (a) 2 and (b) 9 molecules per cage (obtained from MD trajectories; only one layer shown; H atoms are omitted for clarity). Blue and orange colors indicate the CH_4 locations in *lta* cage and *d8r*, respectively. (c) Number of CH_4 molecules located in *lta* cage and *d8r*, as well as the ratio of *lta*/*d8r* in RHO zeolite. (d) Residue time in *lta* cage and *d8r* in RHO zeolite.

2.3. Free Energy. To understand the effect of loading on diffusion behavior, the free energy profile of the diffusion molecule must be analyzed.[24,32] Here, we developed a 3D diffusion free energy method (see Computatinal and Experimental Methods), which can provide information for realistic diffusion paths and diffusion energy barriers as well as consider effects of temperature and concentration, to reveal the diffusion mechanism in cage-type zeolites. Figure 4a shows the 3D free energy map of diffusion for 1 methane per cage in RHO zeolite at 298 K. This indicates that methane migrated along the pore wall of zeolites with low free energy. Based on the 3D free energy maps, the 2D free energy map (Figure 4b) was extracted to quantify the diffusion paths and diffusion free energy barriers. The 2D free energy map indicates that CH_4 moves along the wall (purple dots) rather than the center of the *lta* cage (with high free energy), which is consistent with the interaction energy profile (Figure 3c). In addition, it should be noted that *d8r* is the only channel between two neighboring *lta* cages for molecules to pass (Figure 3a), which is like a door between rooms. Based on the 2D free energy map, we plotted the 1D free energy profile along the diffusion pathway, and the corresponding local minima sites are presented in Figure 4c. Three different adsorption sites are clearly presented: at the center of *d8r* (sites *a* and *a*′), at the mouth of the *lta* cage (sites *c* and *c*′), and at the corner of the *lta* cage (site *e*) (Figure 4b). Apparently, the preferential adsorption site in *d8r* possesses the lowest free energy, consistent with the interaction energy (Figure 3c).

As for the free energy at various loadings, the 1D maps are very similar but the free energy barriers are different. As shown in Figure 4d, there are four different diffusion barriers codetermine the free energy profile. Obviously, the diffusion barriers from *d8r* (*a* to *b*) and the variations of diffusion barriers from the mouth of the *lta* cage (*b* to *c*) are the largest. At lower loading (e.g., 1−9 molecules per cage), the diffusion coefficient decreases because the diffusion barrier from the *d8r* (see a to b in Figure 4d) is almost the same, whereas that from the eight-member ring to the mouth of the *lta* cage (*b* to *c*) increases. Thus, more methane molecules tend to locate at the mouth of the *lta* cage after collision with the molecule preferentially occupying the *d8r*. Therefore, the molecules hinder each other by forming gates themselves. However, as more molecules aggregate, the diffusion accelerates due to the rapid drop of the free energy barrier from *d8r* (see a to b in Figure 4d), which indicates that the molecules will cooperate with each other and pull the gate open. Due to the absence of the *d8r* from the LTA zeolite, the diffusion trend is reversed (Figure S4 in Supporting Information). Overall, the diffusion behaviors are strongly correlated to the eight-membered ring of RHO and LTA zeolites.

2.4. Distribution of Cage Occupancy and Residue Time. In addition, we also studied the number of molecules (population) located in both the *lta* cage and *d8r*, which was previously shown to affect diffusion as a function of loading.[31] Within the investigated loading range (1−12 molecules per cage), a competitive adsorption phenomenon is observed (Figure 5a−c). For example, CH_4 molecules prefer adsorption in *d8r*s (orange) at low loading (Figure 5a), while they tend to locate in *lta* cages (blue) due to the saturation of *d8r* at high loading (Figure 5b). We ascribe the preferential adsorption in *d8r* to the strong adsorption structure at a low loading. Meanwhile, the large population of CH_4 molecules in the *lta* cage is due to accessibility at high loading (Figure 5c, >9 molecules per cage). Interestingly, the turning point of diffusion (Figure 2c) corresponds to a *lta*/*d8r* population ratio equal to 2 (Figure 5c, 9 molecules per cage), indicating

https://doi.org/10.1021/jacs.4c17510
J. Am. Chem. Soc. 2025, 147, 6126−6136

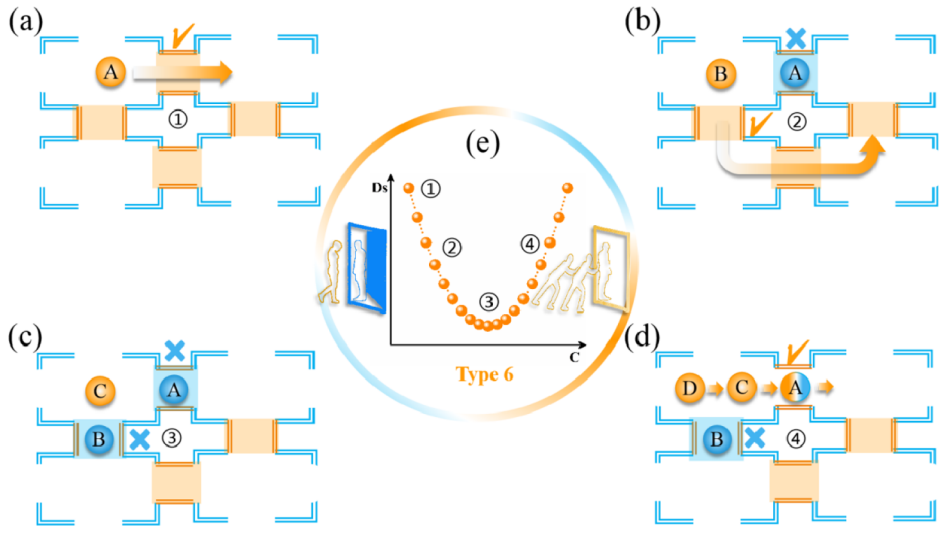

Figure 6. Mechanism of molecular self-gating controlled diffusion in RHO zeolite at low loading (a–c) and high loading (d), along with the variation of diffusion coefficient (e).

that more than two molecules located in the *lta* cage will synergistically open the door (one molecule located in *d8r*) and then promote diffusion, which was confirmed by the following analysis of the radial distribution function and residue time.

The residue time (T_r), where one molecule continuously stays in *lta* or *d8r* of the RHO zeolite, was obtained (Figure 5d). Surprisingly, the T_r in *d8r* remains almost constant (ca. 300 ps), while it monotonically increases in the *lta* cage when the loading is less than 9: the T_r in *lta* is 81, 269, and 566 ps at loadings of 1, 5, and 9 molecules per cage, respectively. Thus, the molecules may obstruct each other and cause a "traffic jam" that increases the residence time in the *lta* cage, whereas there is no such effect in *d8r*. The radial distribution function indicates that methane molecules are more dispersed when the loading is less than 9 (Figure S5 in Supporting Information). However, as the loading increases to greater than 9 molecules per cage, molecules are more concentrated in the first peak near 4 Å (Figure S5 in Supporting Information), which presents "smooth traffic" as the residue time in both *lta* (from 531 to 87 ps) and *d8r* (from 309 to 29 ps) is decreased sharply (Figure 5d). Overall, the D_s first decreases due to the increasing residue time in the *lta* cage with a more decentralized state, but D_s increases as the loading increases because of the decreasing residue time in both *lta* and *d8r* with a more centralized state.

2.5. Molecular Self-Gating Controlled Diffusion. It is well-known that zeolites experience a phenomenon called the "molecular trapdoor" or "molecular gate effect", in which a cation located in an energetically favorable site near the window forms a trapdoor or the window is changed to selectively admit gases.[33−40] Most examples of the "molecular gate effect" have been induced by external conditions, such as adding other cations or changing the temperature. In electrocatalysis, He et al. found that the electrocatalytic reaction itself can strongly modulate the surface conductance of semiconductor electrocatalysts in a process defined as "self-gating".[41] Here, the diffusion was spontaneously induced by the adsorbate itself, leading us to suggest a novel mechanism to explain the diffusion behaviors by a unique "molecule self-gating effect."

At very low loading (e.g., 1 molecule per cage), the transport of methane (see orange ball A in Figure 6a) is fast, as there is no obstacle from other molecules on the diffusion path. Importantly, *d8r*, which connects two adjacent *lta* cages, is the only composite building unit for molecule transport. Based on the unique structure (Figure 2a) and interaction energy profile (Figure 3c) of RHO, the molecule preference for binding inside the *d8r* (see blue ball A in Figure 6b) is due to a stronger interaction (Figure 3c), which, as loading increases, forms a gate that obstructs the diffusion of other molecules (see orange ball B in Figure 6b). Then, the diffusion slows as more gates form (blue balls A and B in Figure 6c). However, as the loading increases to some threshold value (i.e., 9 molecules per cage), the diffusion coefficients increase because several molecules (see orange balls D and C in Figure 6d) synergistically open the gate (see orange and blue balls A in Figure 6d). This self-gating controlled diffusion with a "traffic jam" and "smooth traffic" has also been verified by the free energy and residue time. Figure 5d shows that, at low loading (less than 9 molecules per cage), the residue time (T_r) of the molecule in *d8r* is almost constant because the free energy barrier jumping out of the *d8r* is invariant (see a-b in Figure 4d), while T_r rapidly increases in the *lta* cage because of the increasing corresponding energy barrier (see b-c in Figure 4d). This result indicates that the time for the door opening and closing was invariable because of the "traffic jam" at low loading. However, as the loading increases to 9, the free energy barriers for the *d8r* and *lta* immediately drop (Figure 4d), and the residue time for both the *d8r* and *lta* cage decreases, indicating the "smooth traffic" caused by the opened gate.

In addition, the robustness of this diffusion behavior was investigated. As shown in Figure S6 in Supporting Information, the molecular self-gating controlled diffusion was also present at other temperatures (e.g., 150 and 450 K), which supports our speculation that molecular self-gating effect is not only present at normal temperature, it can occur at other temperatures as well. The flexibility of the framework has been considered[34,42], the diffusion coefficient in flexible RHO zeolite is 2.55×10^{-9}, 0.48×10^{-9} and 1.43×10^{-9} m^2/s at the loading number of 1, 9, and 12 molecule per cage, respectively (Figure S7 in Supporting Information). Besides CH_4, the

https://doi.org/10.1021/jacs.4c17510
J. Am. Chem. Soc. 2025, 147, 6126−6136

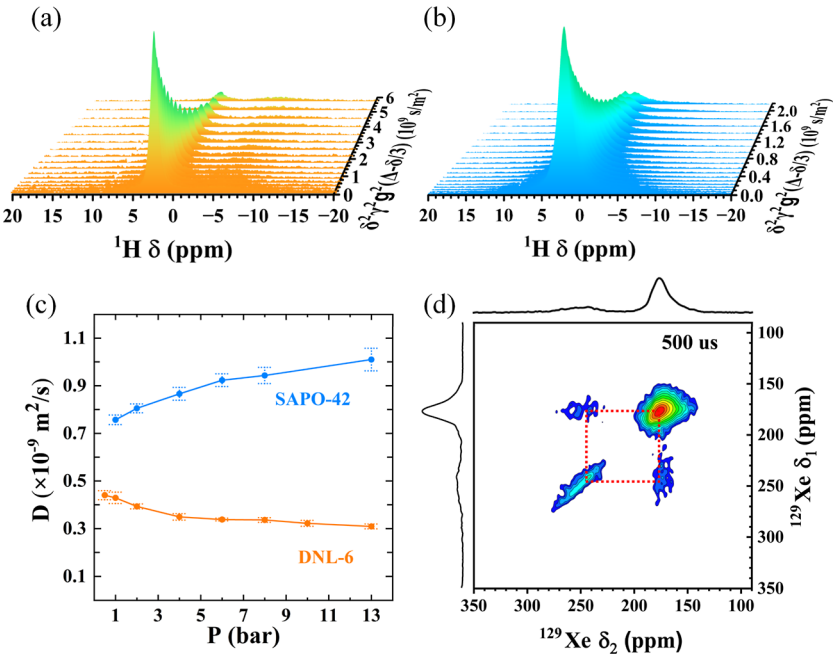

Figure 7. ^{1}H PFG NMR attenuations of (a) DNL-6 (RHO) and (b) SAPO-42 (LTA) molecular sieves under 1.0 bar methane adsorption at 298 K as a function of $(\gamma\delta g)^2\left(\Delta - \frac{\delta}{3}\right)$, respectively. γ, δ, g, and Δ represent the gyromagnetic ratio of the ^{1}H nucleus, effective gradient pulse duration, gradient strength, and diffusion time, respectively. (c) Loading dependence of self-diffusion coefficients for methane in the two molecular sieves at 298 K by the PFG NMR experiment. (d) 2D ^{129}Xe EXSY NMR spectrum of Xenon in the DNL-6 molecular sieve acquired at 154 K using a mixing time of 500 μs. The xenon gas enriched with ^{129}Xe (80% enrichment) was introduced into a 5 mm pressure-valved NMR tube to a pressure of 0.9 bar at 298 K.

diffusion also occurred for other molecules such as Xe (Figure S8 in Supporting Information). Furthermore, it also happened in AlPO-type (different composition) RHO (Figure S8 in Supporting Information) and MER (different topology, see Figure S1c in Supporting Information) zeolites with *d8r* (Figure S9 in Supporting Information), which indicates the robustness of molecular self-gating control diffusion in zeolites with a *d8r* structure (as the only access). However, due to the absence of the *d8r* structure, there is no molecular self-gating control diffusion in zeolites with UFI (Figures S1d and S10 in Supporting Information), CHA (Figure S11a,c in Supporting Information) and FAU topologies (Figure S11b,d in Supporting Information).

To further prove the molecular self-gating controlled diffusion in RHO topologic zeolite, pulsed field gradient (PFG) NMR, a well-suited tool for intracrystalline D_s measurement,[43,44] was utilized to measure the self-diffusion coefficient of methane in RHO (DNL-6) and LTA (SAPO-42) topological silicoaluminophosphate (SAPO) molecular sieves. Figure 7a,b displays the typical ^{1}H PFG NMR attenuations of methane in DNL-6 and SAPO-42 molecular sieves as a function of $(\gamma\delta g)^2\left(\Delta - \frac{\delta}{3}\right)$, respectively, demonstrating that the methane D_s in DNL-6 is smaller than that in SAPO-42 as methane in DNL-6 requires a stronger strength of gradient field (i.e., larger value of $(\gamma\delta g)^2\left(\Delta - \frac{\delta}{3}\right)$) at an equivalent degree of attenuation. In both cases of DNL-6 and SAPO-42, the attenuations fit well with the Stejskal−Tanner equation (eq 5). The loading dependences of the self-diffusion coefficients for methane in two molecular sieves at 298 K are shown in Figure 7c. The D_s in DNL-6 decreased with the increasing pressure from 0.5 to 13.0 bar, while that in SAPO-42 monotonically increased (consistent with the diffusion behavior for general cage-type zeolite[16]). Although the methane adsorption amounts of samples could not be achieved at higher loadings due to the pressure limitations of the NMR tube, the trends in D_s for both molecular sieves align closely with the MD simulations at low methane loadings. In addition, the "traffic jam" effect resulting from the confinement within *d8r* is validated by ^{129}Xe NMR experiments.

It is noteworthy that, the ^{1}H and ^{13}C chemical shifts of CH_4 are not sensitive to the adsorbed environment; fortunately, ^{129}Xe NMR was alternatively selected to confirm the "traffic jam" effect of *d8r* on adsorption and diffusion behaviors due to its large electron cloud density and high susceptibility to polarization from the zeolite framework.[45−48] As shown in Figure S14, SAPO-42 consistently displays a single ^{129}Xe signal under 0.9 bar (the pressure measured at 298 K), as the *lta* cage is the sole adsorption site in the framework. The higher chemical shift of the ^{129}Xe NMR signal results from the increased xenon adsorption numbers with decreasing temperature. In contrast, the sharp ^{129}Xe NMR signal in DNL-6 broadens and gradually separates into two signals, located at ca. 175 and 240 ppm, respectively, with temperature decreased to 153 K, demonstrating Xe atoms are exclusively adsorbed in *lta* and *d8r* environments, respectively. At a lower Xe pressure of 0.5 bar (the top red line, adsorption pressure was measured at 298 K and ^{129}Xe NMR spectrum was acquired at 151 K), the relative content of Xe molecule in the *d8r* increases and exceeds that in *lta* cages. It agrees with the calculations that Xe molecules preferentially adsorb in the *d8r* prism and are ready to form a "traffic jam" in the diffusion process. Furthermore, 2D ^{129}Xe exchange spectroscopy (EXSY) NMR was employed to provide dynamic information about the motions of xenon in *d8r* and *lta* cages.[49] Figures 7d and S15 display the 2D ^{129}Xe

https://doi.org/10.1021/jacs.4c17510
J. Am. Chem. Soc. 2025, 147, 6126−6136

EXSY NMR result of xenon in DNL-6 molecular sieve at 154 K with various mixing times. A very weak and separate cross peak in the off-diagonal of spectra emerges with a mixing time of 200 μs (Figure S15b) and the cross peaks become pronounced as the mixing time increases to 500 μs (Figure 7d), indicating extremely slow exchange between Xe atoms in *d8r* and *lta* adsorption sites because of the "traffic jam" effect. It is noteworthy that the more interesting experimental evidence of diffusion behavior (smooth traffic) has remained a great challenge thus far due to the extremely high-pressure NMR instrumentation limitations.

3. CONCLUSIONS

In summary, we have developed a method to quantitatively correlate zeolite structure and diffusion behavior based on 3D free energy and CTRW coarse-graining method, which does not require a prespecified diffusion path and is able to consider the effect of temperature and concentration. Based on this method, we found a novel loading-dependent diffusion behavior where the self-diffusion coefficient first decreases and then increases, and we investigated the mechanism of molecular self-gating control diffusion in RHO cage-type zeolites based on the interaction energy profile, free energy, jump frequency, and residue time. At low loading, the adsorbates will spontaneously form a gate by themselves in the double eight-member ring (*d8r*), which inhibits the movement of other molecules, while the diffusion will be promoted by the effect of synergistically opening the gate at high loading. The novel diffusion has a strong correlation to the composition and topology of zeolite, adsorbent, and temperature. This new transport will enrich the present diffusion behavior. We anticipate that this self-gating effect will be widely adopted to study the selective adsorption and separation as well as be applied in high pressure sensing and storage.

4. COMPUTATIONAL AND EXPERIMENTAL METHODS

4.1. MD Simulation. The initial framework structures of pure silicon (i.e., RHO, LTA, MER, and UFI) were taken from the International Zeolite Associations database[50] and optimized by GULP[51,52] with SLC core−shell force field.[53,54] The selected super cells are 3 × 3 × 3, 4 × 4 × 4, 4 × 4 × 2, and 4 × 4 × 4 for RHO, LTA, MER, and UFI, respectively (see Table S1 in Supporting Information). These cell parameters were used in the MD simulation. All MD simulations were performed in the canonical ensemble (*NVT*), where the number of particles (*N*), volume (*V*), and temperature (*T*) were kept constant. The simulated temperature was held at 300 K and controlled by a Nosé−Hoover thermostat with a coupling time constant of 1 ps. The velocity Verlet algorithm was used to integrate Newton's equations of motion with a time step of 1 fs. Each MD simulation was equilibrated for 5 ns, followed by 100 ns of production for studying the diffusion behavior of methane molecules. The trajectories were recorded every 1000 steps, and 3−17 independent MD simulations were carried out for better statistics. The parameters of force field (see Table S2 in Supporting Information) were given in the original reference by Sholl,[55,56] and the validity has been verified in our previous work.[30] The Lennard-Jones cross-interaction parameter for Xe and zeolite was determined by the Lorentz−Berthelot mixing rules. All Lennard-Jones interactions were calculated with a 12 Å cutoff radius, and periodic boundary conditions were also used in all three directions. MD simulations were performed in the parallel general purpose DL_POLY code.[57]

4.2. Diffusion Coefficient. The mean square displacement (MSD) of adsorbed molecules is defined as the following equation

$$\mathrm{MSD}(\tau) = \frac{1}{N_\mathrm{m}}\sum_{i}^{N_\mathrm{m}}\frac{1}{N_\tau}\sum_{t_0}^{N_\tau}[r_i(t_0+\tau) - r_i(t_0)] \tag{1}$$

where N_m is the number of adsorbed molecules, N_τ is the number of time origins used in calculating the average, and r_i is the coordinate of the center-of-mass of molecule *i*. The slope of the MSD as a function of time determines the self-diffusion coefficient, D_s, defined according to the so-called Einstein relation[58]

$$\mathrm{MSD}(\tau) = 2nD_s\tau + b \tag{2}$$

where *n* is the dimension of frameworks (*n* = 3, 3, 3, and 1 for RHO, LTA, UFI, and MER, respectively), and *b* is the thermal factor arising from atomic vibrations. The line was fitted in the range of 1000−5000 ps using a least-squares fit. The reported MSD curves and corresponding D_s values were calculated as the average of 3 to 17 independent MD trajectories.

4.3. Free Energy. The free energy profile is a reliable method to explain the diffusion behavior of a hydrocarbon molecule passing through zeolites. First, the 3D probability density was generated from the trajectories of 51^3 point meshes. To improve the statistics of our calculations, all densities were projected into one unit cell. The normalized histogram of trajectory $\zeta(t)$ is the probability distribution $P(\zeta)$ of the gas. Here, ζ represents the 3D coordinate of the center of mass of the molecule. By taking the logarithm of $P(\zeta)$, the free energy profile $F(\zeta) = -k_\mathrm{B}T \times \ln P(\zeta)$ is obtained up to an arbitrary constant, where T and k_B are the temperature and the Boltzmann constant, respectively. Then, the 2D free energy map was extracted from the center of the 3D free energy maps. Finally, the 1D free energy curve along the diffusion path with 51 local minimum points was extracted from the 2D free energy map.

4.4. Continuous-Time Random-Walk Coarse-Graining Method.[30,59] In the coarse-graining time algorithm, the center of the *k*-th dynamic basin of the tagged methane molecule, $\bar{R}(n)_k$, is done iteratively as

$$\bar{R}(n)_k = \frac{(n-1)\bar{R}(n-1)_k + R(n)}{n} \tag{3}$$

The average is updated until $R(n+1)$ walks out of a certain range

$$|R(n+1) - \bar{R}(n)_k| \begin{cases} \le D_{\max} & \text{update the basic center position} \\ > D_{\max} & \text{start the new basin} \end{cases} \tag{4}$$

$D_{\max}$ was set to 11 and 13 Å, which was found to be a reasonable value for methane, as a threshold of the basin crossing in LTA and RHO, respectively. The past *n* snapshots are defined as a dynamical basin centered at $\bar{R}(n)_k$. If the labeled molecule hops into a new basin according to eq 4, the running index *n* is updated to 1. The hopping frequency *f* is defined as the number of jumps for methane from one dynamic basin to another, while the jump length *L* is the average distance between two consecutive basin centers $\langle \bar{R}_{k+1} - \bar{R}_k \rangle$.

4.5. Pulsed-Field Gradient NMR. The scheme outlining the sample preparation process for NMR experiments is presented in Supporting Information Figure S16. PFG NMR measurements were conducted on a Bruker AVANCE III 600 spectrometer equipped with a 14.1 T wide-bore magnet. A 5 mm diff50 probe was used, providing the maximum gradient strength of 1800 G/cm in the *z*-direction. A bipolar-gradient stimulated echo sequence (STEBP)[60,61] was applied in diffusion measurements to eliminate the effect of magnetic susceptibility in the beds of SAPO materials (Figure S17a). Optimal parameters (δ, *g*, and Δ) were set for each PFG NMR test. The intracrystalline D_s is determined using eq 5,[61] as the linear fittings of semilogarithmic plots for the attenuation of I/I_0 are shown in Figure S17b,c.

$$I = I_0 \exp\left[-(\gamma\delta g)^2 D\left(\Delta - \frac{\delta}{3}\right)\right] \tag{5}$$

https://doi.org/10.1021/jacs.4c17510
J. Am. Chem. Soc. 2025, 147, 6126−6136

where I and I_0 are the signal amplitudes with and without gradient field strength, respectively. The echo signals decayed exponentially as the gradient strength (g) increased linearly, while the diffusion time (Δ) and effective gradient pulse duration (δ) remained constant. γ is the gyromagnetic ratio of the ^{1}H nucleus. The attenuations of I/I_0 for both samples fitted well with the Stejskal−Tanner equation, indicating a standard three-dimensional isotropic diffusion.

■ ASSOCIATED CONTENT

Supporting Information

The Supporting Information is available free of charge at https://pubs.acs.org/doi/10.1021/jacs.4c17510.

Additional details of samples and characterization, ^{129}Xe NMR experiment, computational details of interaction energy profile and diffusion radius, comparison of trajectories, and structural and radial distribution function at various loading (PDF)

■ AUTHOR INFORMATION

Corresponding Authors

Zhiqiang Liu − *Interdisciplinary Institute of NMR and Molecular Sciences, Hubei Province for Coal Conversion and New Carbon Materials, School of Chemistry and Chemical Engineering, Wuhan University of Science and Technology, Wuhan 430081, P. R. China*; Email: zqliu_wh@wust.edu.cn

Shutao Xu − *National Engineering Research Center of Lower-Carbon Catalysis Technology, Dalian Institute of Chemical Physics, Chinese Academy of Sciences, Dalian 116023, P. R. China*; orcid.org/0000-0003-4722-8371; Email: xushutao@dicp.ac.cn

Anmin Zheng − *Interdisciplinary Institute of NMR and Molecular Sciences, Hubei Province for Coal Conversion and New Carbon Materials, School of Chemistry and Chemical Engineering, Wuhan University of Science and Technology, Wuhan 430081, P. R. China; State Key Laboratory of Magnetic Resonance Spectroscopy and Imaging, Innovation Academy for Precision Measurement Science and Technology, Chinese Academy of Sciences, 430071 Wuhan, P. R. China*; orcid.org/0000-0001-7115-6510; Email: zhenganm@wipm.ac.cn

Authors

Caiyi Lou − *National Engineering Research Center of Lower-Carbon Catalysis Technology, Dalian Institute of Chemical Physics, Chinese Academy of Sciences, Dalian 116023, P. R. China; University of Chinese Academy of Sciences, 100049 Beijing, P. R. China*; orcid.org/0000-0001-6204-0022

Jiamin Yuan − *State Key Laboratory of Magnetic Resonance Spectroscopy and Imaging, Innovation Academy for Precision Measurement Science and Technology, Chinese Academy of Sciences, 430071 Wuhan, P. R. China*

Xiaomin Tang − *State Key Laboratory of Magnetic Resonance Spectroscopy and Imaging, Innovation Academy for Precision Measurement Science and Technology, Chinese Academy of Sciences, 430071 Wuhan, P. R. China*; orcid.org/0000-0002-5651-4444

Yuzhou Fan − *University of Chinese Academy of Sciences, 100049 Beijing, P. R. China; State Key Laboratory of Magnetic Resonance Spectroscopy and Imaging, Innovation Academy for Precision Measurement Science and Technology, Chinese Academy of Sciences, 430071 Wuhan, P. R. China*

Ji Qi − *Interdisciplinary Institute of NMR and Molecular Sciences, Hubei Province for Coal Conversion and New Carbon Materials, School of Chemistry and Chemical Engineering, Wuhan University of Science and Technology, Wuhan 430081, P. R. China*

Rui Zhang − *Interdisciplinary Institute of NMR and Molecular Sciences, Hubei Province for Coal Conversion and New Carbon Materials, School of Chemistry and Chemical Engineering, Wuhan University of Science and Technology, Wuhan 430081, P. R. China*

Peng Peng − *Interdisciplinary Institute of NMR and Molecular Sciences, Hubei Province for Coal Conversion and New Carbon Materials, School of Chemistry and Chemical Engineering, Wuhan University of Science and Technology, Wuhan 430081, P. R. China*; orcid.org/0000-0002-8258-6812

Guoliang Liu − *Interdisciplinary Institute of NMR and Molecular Sciences, Hubei Province for Coal Conversion and New Carbon Materials, School of Chemistry and Chemical Engineering, Wuhan University of Science and Technology, Wuhan 430081, P. R. China*

Complete contact information is available at: https://pubs.acs.org/10.1021/jacs.4c17510

Author Contributions

$^{\perp}$Z.L. and C.L. contributed equally to this work. All authors have given approval to the final version of the manuscript.

Notes

The authors declare no competing financial interest.

■ ACKNOWLEDGMENTS

This work was supported by the National Key R&D Program of China (nos. 2023YFA1507700, 2022YFE0116000, and 2021YFA1502600), the National Natural Science Foundation of China (nos. 22202215, 22125304, 22032005, 22241801, 22208337, 22002174, 22022804, and 22378064), the Natural Science Foundation of Hubei Province (2024AFA054), and the Natural Science Foundation of Wuhan (2024040701010058). Numerical calculation is supported by High-Performance Computing Center of Wuhan University of Science and Technology.

■ REFERENCES

(1) Bunde, A.; Caro, J.; Kärger, J.; Vogl, G. *Diffusive Spreading in Nature, Technology and Society*; Springer: Cham, Switzerland, 2018.

(2) Jarenwattananon, N. N.; Glöggler, S.; Otto, T.; Melkonian, A.; Morris, W.; Burt, S. R.; Yaghi, O. M.; Bouchard, L. S. Thermal Maps of Gases in Heterogeneous Reactions. *Nature* **2013**, *502* (7472), 537−540.

(3) Kärger, J.; Valiullin, R. Mass Transfer in Mesoporous Materials: the Benefit of Microscopic Diffusion Measurement. *Chem. Soc. Rev.* **2013**, *42* (9), 4172−4197.

(4) Chmelik, C.; Kärger, J. In Situ Study on Molecular Diffusion Phenomena in Nanoporous Catalytic Solids. *Chem. Soc. Rev.* **2010**, *39* (12), 4864−4884.

(5) Krishna, R. Diffusion in Porous Crystalline Materials. *Chem. Soc. Rev.* **2012**, *41* (8), 3099−3118.

(6) Burada, P. S.; Hänggi, P.; Marchesoni, F.; Schmid, G.; Talkner, P. Diffusion in Confined Geometries. *ChemPhysChem* **2009**, *10* (1), 45−54.

(7) Dubbeldam, D.; Calero, S.; Maesen, T. L. M.; Smit, B. Incommensurate Diffusion in Confined Systems. *Phys. Rev. Lett.* **2003**, *90* (24), 245901.

(8) Gu, C.; Hosono, N.; Zheng, J. J.; Sato, Y.; Kusaka, S.; Sakaki, S.; Kitagawa, S. Design and Control of Gas Diffusion Process in a Nanoporous Soft Crystal. *Science* **2019**, *363* (6425), 387−391.
(9) Zhou, H. C.; Long, J. R.; Yaghi, O. M. Introduction to Metal-Organic Frameworks. *Chem. Rev.* **2012**, *112* (2), 673−674.
(10) Breck, D. W. *Zeolite Molecular Sieves: Structure, Chemistry, and Use*; Wiley: New York, 1973.
(11) Sholl, D. S.; Lively, R. P. Seven Chemical Separations to Change the World. *Nature* **2016**, *532* (7600), 435−437.
(12) Sun, M. H.; Huang, S. Z.; Chen, L. H.; Li, Y.; Yang, X. Y.; Yuan, Z. Y.; Su, B. L. Applications of Hierarchically Structured Porous Materials from Energy Storage and Conversion, Catalysis, Photocatalysis, Adsorption, Separation, and Sensing to Biomedicine. *Chem. Soc. Rev.* **2016**, *45* (12), 3479−3563.
(13) Jin, Z.; Wang, L.; Zuidema, E.; Mondal, K.; Zhang, M.; Zhang, J.; Wang, C. T.; Meng, X. J.; Yang, H. Q.; Mesters, C.; et al. Hydrophobic Zeolite Modification for in Situ Peroxide Formation in Methane Oxidation to Methanol. *Science* **2020**, *367* (6474), 193−197.
(14) Beerdsen, E.; Dubbeldam, D.; Smit, B. Molecular Understanding of Diffusion in Confinement. *Phys. Rev. Lett.* **2005**, *95* (16), 164505.
(15) Jakobtorweihen, S.; Verbeek, M. G.; Lowe, C. P.; Keil, F. J.; Smit, B. Understanding the Loading Dependence of Self-Diffusion in Carbon Nanotubes. *Phys. Rev. Lett.* **2005**, *95* (4), 044501.
(16) Beerdsen, E.; Dubbeldam, D.; Smit, B. Understanding Diffusion in Nanoporous Materials. *Phys. Rev. Lett.* **2006**, *96* (4), 044501.
(17) Beerdsen, E.; Smit, B.; Dubbeldam, D. Molecular Simulation of Loading Dependent Slow Diffusion in Confined Systems. *Phys. Rev. Lett.* **2004**, *93* (24), 248301.
(18) Dubbeldam, D.; Beerdsen, E.; Vlugt, T. J. H.; Smit, B. Molecular Simulation of Loading-Dependent Diffusion in Nanoporous Materials Using Extended Dynamically Corrected Transition State Theory. *J. Chem. Phys.* **2005**, *122* (22), 224712.
(19) Karger, J.; Pfeifer, H. NMR Self-Diffusion Studies in Zeolite Science and Technology. *Zeolites* **1987**, *7* (2), 90−107.
(20) Beerdsen, E.; Dubbeldam, D.; Smit, B. Loading Dependence of The Diffusion Coefficient of Methane in Nanoporous Materials. *J. Phys. Chem. B* **2006**, *110* (45), 22754−22772.
(21) Germanus, A.; Karger, J.; Pfeifer, H. Self-Diffusion of Paraffins and Olefins in Zeolite Na-X under the Influence of Residual Water-Molecules. *Zeolites* **1984**, *4* (2), 188−190.
(22) Germanus, A.; Karger, J.; Pfeifer, H.; Samulevic, N. N.; Zdanov, S. P. Intracrystalline Self-Diffusion of Benzene, Toluene and Xylene Isomers in Zeolites Na-X. *Zeolites* **1985**, *5* (2), 91−95.
(23) Pfeifer, H.; Karger, J.; Germanus, A.; Schirmer, W.; Bülow, M.; Caro, J. Concentration Dependence of Intracrystalline Self-Diffusion in Zeolites. *Adsorpt. Sci. Technol.* **1985**, *2*, 229−239.
(24) Amirjalayer, S.; Schmid, R. Mechanism of Benzene Diffusion in MOF-5: A Molecular Dynamics Investigation. *Microporous Mesoporous Mater.* **2009**, *125* (1−2), 90−96.
(25) Smit, B.; Maesen, T. L. M. Molecular Simulations of Zeolites: Adsorption, Diffusion, and Shape Selectivity. *Chem. Rev.* **2008**, *108* (10), 4125−4184.
(26) Cnudde, P.; Demuynck, R.; Vandenbrande, S.; Waroquier, M.; Sastre, G.; Speybroeck, V. V. Light Olefin Diffusion during the MTO Process on H-SAPO-34: A Complex Interplay of Molecular Factors. *J. Am. Chem. Soc.* **2020**, *142* (13), 6007−6017.
(27) Ghorai, P. K.; Yashonath, S.; Demontis, P.; Suffritti, G. B. Diffusion Anomaly as a Function of Molecular Length of Linear Molecules: Levitation Effect. *J. Am. Chem. Soc.* **2003**, *125* (23), 7116−7123.
(28) Nag, S.; Ananthakrishna, G.; Maiti, P. K.; Yashonath, S. Separating Hydrocarbon Mixtures by Driving the Components in Opposite Directions: High Degree of Separation Factor and Energy Efficiency. *Phys. Rev. Lett.* **2020**, *124*, 255901.
(29) Robson, H. E.; Shoemake, D. P.; Ogilvie, R. A.; Manor, P. C. Synthesis and Crystal-Structure of Zeolite Rho - New Zeolite Related to Linde Type-A. In *Molecular Sieves*; *Advances in Chemistry*; American Chemical Society, 1973; Vol. *121*, pp 106−115.
(30) Gao, S. S.; Liu, Z. Q.; Xu, S. T.; Zheng, A. M.; Wu, P. F.; Li, B.; Yuan, X. S.; Wei, Y. X.; Liu, Z. M. Cavity-Controlled Diffusion in 8-Membered Ring Molecular Sieve Catalysts for Shape Selective Strategy. *J. Catal.* **2019**, *377*, 51−62.
(31) Liu, Z. Q.; Yuan, J. M.; van Baten, J. M.; Zhou, J.; Tang, X. M.; Zhao, C.; Chen, W.; Yi, X. F.; Krishna, R.; Sastre, G.; Zheng, A. M. Synergistically Enhance Confined Diffusion by Continuum Intersecting Channels in Zeolites. *Sci. Adv.* **2021**, *7* (11), No. eabf0775.
(32) Amirjalayer, S.; Tafipolsky, M.; Schmid, R. Molecular Dynamics Simulation of Benzene Diffusion in MOF-5: Importance of Lattice Dynamics. *Angew. Chem., Int. Ed.* **2007**, *46* (3), 463−466.
(33) Shang, J.; Li, G.; Singh, R.; Gu, Q. F.; Nairn, K. M.; Bastow, T. J.; Medhekar, N.; Doherty, C. M.; Hill, A. J.; Liu, J. Z.; Webley, P. A. Discriminative Separation of Gases by a "Molecular Trapdoor" Mechanism in Chabazite Zeolites. *J. Am. Chem. Soc.* **2012**, *134* (46), 19246−19253.
(34) Lozinska, M. M.; Mangano, E.; Mowat, J. P. S.; Shepherd, A. M.; Howe, R. F.; Thompson, S. P.; Parker, J. E.; Brandani, S.; Wright, P. A. Understanding Carbon Dioxide Adsorption on Univalent Cation Forms of the Flexible Zeolite Rho at Conditions Relevant to Carbon Capture from Flue Gases. *J. Am. Chem. Soc.* **2012**, *134* (42), 17628−17642.
(35) Lozinska, M. M.; Mowat, J. P. S.; Wright, P. A.; Thompson, S. P.; Jorda, J. L.; Palomino, M.; Valencia, S.; Rey, F. Cation Gating and Relocation during the Highly Selective "Trapdoor" Adsorption of CO2 on Univalent Cation Forms of Zeolite Rho. *Chem. Mater.* **2014**, *26* (6), 2052−2061.
(36) Kuznicki, S. M.; Bell, V. A.; Nair, S.; Hillhouse, H. W.; Jacubinas, R. M.; Braunbarth, C. M.; Toby, B. H.; Tsapatsis, M. A Titanosilicate Molecular Sieve with Adjustable Pores for Size-Selective Adsorption of Molecules. *Nature* **2001**, *412* (6848), 720−724.
(37) De Baerdemaeker, T.; De Vos, D. Gas Separation Trapdoors in Zeolites. *Nat. Chem.* **2013**, *5* (2), 89−90.
(38) Bai, R. B.; Song, X. W.; Yan, W. F.; Yu, J. H. Low-Energy Adsorptive Separation by Zeolites. *Natl. Sci. Rev.* **2022**, *9* (9), nwac064.
(39) Georgieva, V. M.; Bruce, E. L.; Verbraeken, M. C.; Scott, A. R.; Casteel, W. J.; Brandani, S.; Wright, P. A. Triggered Gate Opening and Breathing Effects during Selective CO Adsorption by Merlinoite Zeolite. *J. Am. Chem. Soc.* **2019**, *141* (32), 12744−12759.
(40) Zhao, J. H.; Mousavi, S. H.; Xiao, G. K.; Mokarizadeh, A. H.; Moore, T.; Chen, K. F.; Gu, Q. F.; Singh, R.; Zavabeti, A.; Liu, J. Z.; Webley, P. A.; Li, G. K. Nitrogen Rejection from Methane via a "Trapdoor" K-ZSM-25 Zeolite. *J. Am. Chem. Soc.* **2021**, *143* (37), 15195−15204.
(41) He, Y. M.; He, Q. Y.; Wang, L. Q.; Zhu, C.; Golani, P.; Handoko, A. D.; Yu, X. C.; Gao, C. T.; Ding, M. N.; Wang, X. W.; Liu, F. C.; Zeng, Q. S.; Yu, P.; Guo, S. S.; Yakobson, B. I.; Wang, L.; Seh, Z. W.; Zhang, Z. H.; Wu, M. H.; Wang, Q. J.; Zhang, H.; Liu, Z. Self-Gating in Semiconductor Electrocatalysis. *Nat. Mater.* **2019**, *18* (10), 1098−1104.
(42) Clatworthy, E. B.; Moldovan, S.; Nakouri, K.; Gramatikov, S. P.; Dalena, F.; Daturi, M.; Petkov, P. St.; Vayssilov, G. N.; Mintova, S. Visualizing the Flexibility of RHO Nanozeolite: Experiment and Modeling. *J. Am. Chem. Soc.* **2023**, *145* (28), 15313−15323.
(43) Kortunov, P.; Vasenkov, S.; Kärger, J.; Valiullin, R.; Gottschalk, P.; Fé Elía, M.; Perez, M.; Stöcker, M.; Drescher, B.; McElhiney, G.; Berger, C.; Gläser, R.; Weitkamp, J. The Role of Mesopores in Intracrystalline Transport in USY Zeolite: PFG NMR Diffusion Study on Various Length Scales. *J. Am. Chem. Soc.* **2005**, *127* (37), 13055−13059.
(44) Forse, A. C.; Gonzalez, M. I.; Siegelman, R. L.; Witherspoon, V. J.; Jawahery, S.; Mercado, R.; Milner, P. J.; Martell, J. D.; Smit, B.; Blümich, B.; Long, J. R.; Reimer, J. A. Unexpected Diffusion Anisotropy of Carbon Dioxide in the Metal-Organic Framework Zn_2(Dobpdc). *J. Am. Chem. Soc.* **2018**, *140* (5), 1663−1673.
(45) Qin, Z. X.; Cychosz, K. A.; Melinte, G.; El Siblani, H.; Gilson, J. P.; Thommes, M.; Fernandez, C.; Mintova, S.; Ersen, O.; Valtchev, V.

https://doi.org/10.1021/jacs.4c17510
J. Am. Chem. Soc. 2025, 147, 6126−6136

Opening the Cages of Faujasite-Type Zeolite. *J. Am. Chem. Soc.* **2017**, *139* (48), 17273−17276.
(46) Bonardet, J. L.; Gédéon, A.; Springuel-Huet, M. A.; Fraissard, J., NMR of Physisorbed ^{129}Xe Used as a Probe to Investigate Molecular Sieves. In *Characterization II*, Karge, H. G., Weitkamp, J., Eds.; *Molecular Sieves*; Springer: Berlin, Heidelberg, 2007; Vol. *5*, pp 155−248.
(47) Li, M. H.; Ideta, K.; Hata, K.; Kil, H. S.; Kuroda, K.; Zhai, X. Z.; Nakabayashi, K.; Yoon, S. H.; Miyawaki, J. Reevaluation of the Suitability of ^{129}Xe Nuclear Magnetic Resonance Spectroscopy for Pore Size Determination in Porous Carbon Materials. *J. Am. Chem. Soc.* **2024**, *146* (50), 34401−34412.
(48) Comotti, A.; Bracco, S.; Sozzani, P.; Horike, S.; Matsuda, R.; Chen, J.; Takata, M.; Kubota, Y.; Kitagawa, S. Nanochannels of Two Distinct Cross-Sections in a Porous Al-Based Coordination Polymer. *J. Am. Chem. Soc.* **2008**, *130* (41), 13664−13672.
(49) Comotti, A.; Bracco, S.; Valsesia, P.; Ferretti, L.; Sozzani, P. 2D Multinuclear NMR, Hyperpolarized Xenon and Gas Storage in Organosilica Nanochannels with Crystalline Order in the Walls. *J. Am. Chem. Soc.* **2007**, *129* (27), 8566−8576.
(50) Baerlocher, C.; McCusker, L. B. Database of Zeolite Structures. http://www.iza-structure.org/databases/(accessed Jun, 2016).
(51) Gale, J. D. GULP: A Computer Program for the Symmetry-Adapted Simulation of Solids. *J. Chem. Soc., Faraday Trans.* **1997**, *93* (4), 629−637.
(52) Gale, J. D.; Rohl, A. L. The General Utility Lattice Program (GULP). *Mol. Simul.* **2003**, *29* (5), 291−341.
(53) Sanders, M. J.; Leslie, M.; Catlow, C. R. A. Interatomic Potentials for SiO2. *J. Chem. Soc., Chem. Commun.* **1984**, No. 19, 1271−1273.
(54) Catlow, C. R. A.; Freeman, C. M.; Vessal, B.; Tomlinson, S. M.; Leslie, M. Molecular Dynamics Studies of Hydrocarbon Diffusion in Zeolites. *J. Chem. Soc., Faraday Trans.* **1991**, *87* (13), 1947−1950.
(55) Jee, S. E.; Sholl, D. S. Carbon Dioxide and Methane Transport in DDR Zeolite: Insights from Molecular Simulations into Carbon Dioxide Separations in Small Pore Zeolites. *J. Am. Chem. Soc.* **2009**, *131* (22), 7896−7904.
(56) Skoulidas, A. I.; Sholl, D. S. Transport Diffusivities of CH4, CF4, He, Ne, Ar, Xe, and SF6 in Silicalite from Atomistic Simulations. *J. Phys. Chem. B* **2002**, *106* (19), 5058−5067.
(57) Smith, W.; Forester, T. R. DL_POLY_2.0: A General-Purpose Parallel Molecular Dynamics Simulation Package. *J. Mol. Graphics* **1996**, *14* (3), 136−141.
(58) Frenkel, D.; Smit, B. Chapter 4 - Molecular Dynamics Simulations. In *Understanding Molecular Simulation*, 2 ed.; Frenkel, D., Smit, B., Eds.; Academic Press: San Diego, 2002; pp 63−107.
(59) Zhang, Q.; Wu, T.; Chen, C.; Mukamel, S.; Zhuang, W. Molecular Mechanism of Water Reorientational Slowing Down in Concentrated Ionic Solutions. *Proc. Natl. Acad. Sci. U.S.A.* **2017**, *114* (38), 10023−10028.
(60) Cotts, R. M.; Hoch, M. J. R.; Sun, T.; Markert, J. T. Pulsed Field Gradient Stimulated Echo Methods for Improved NMR Diffusion Measurements in Heterogeneous Systems. *J. Magn. Reson.* **1989**, *83* (2), 252−266.
(61) Karger, J. Transport Phenomena in Nanoporous Materials. *ChemPhysChem* **2015**, *16* (1), 24−51.

https://doi.org/10.1021/jacs.4c17510
J. Am. Chem. Soc. 2025, 147, 6126−6136